scientific reports

Check for updates

OPEN

Simplified synthesis and identification of novel nanostructures consisting of cobalt borate and cobalt oxide for crystal violet dye removal from aquatic environments

Asma S. Al-Wasidi[1], Hesham H. El-Feky[2]✉, Reem K. Shah[3], Fawaz A. Saad[3] & Ehab A. Abdelrahman[2,4]✉

Crystal violet dye poses significant health risks to humans, including carcinogenic and mutagenic effects, as well as environmental hazards due to its persistence and toxicity in aquatic ecosystems. This study focuses on the efficient removal of crystal violet dye from aqueous media using novel Co_3O_4/$Co_3(BO_3)_2$ nanostructures synthesized via the Pechini sol–gel approach. The nanostructures, which were abbreviated to EN600 and EN800, were fabricated at calcination temperatures of 600 and 800 °C, respectively. X-ray diffraction (XRD) analysis revealed that the synthesized samples have a cubic Co_3O_4 phase and an orthorhombic $Co_3(BO_3)_2$ phase, with mean crystal sizes of 43.82 nm and 52.93 nm for EN600 and EN800 samples, respectively. The Brunauer–Emmett–Teller (BET) surface areas of EN600 and EN800 samples were 65.80 and 43.76 m^2/g, respectively, indicating a significant surface area available for adsorption. Optimal removal of crystal violet dye was achieved at a temperature of 298 K, a contact time of 70 min, and a pH of 10. The maximum adsorption capacities were found to be 284.09 mg/g for EN600 and 256.41 mg/g for EN800, which are notably higher compared to many conventional adsorbents. The adsorption process followed the pseudo-second-order kinetic model and fitted well with the Langmuir isotherm. The adsorption was exothermic, spontaneous, and physical in nature. Moreover, the adsorbents exhibited excellent reusability, retaining high efficiency after multiple regeneration cycles using 6 mol/L hydrochloric acid. These findings highlight the potential of these Co_3O_4/$Co_3(BO_3)_2$ nanostructures as effective and sustainable materials for water purification applications.

Keywords $Co_3(BO_3)_2$/Co_3O_4 nanostructures, Identification, Decontamination, Crystal violet dye

Aquatic contamination with organic chemical dyes is a considerable environmental subject stemming from various industrial activities[1–4]. The primary sources include the textile, leather, paper, and plastics industries, where dyes are extensively used to color products[5,6]. These industries often discharge untreated or inadequately treated effluents containing high concentrations of dyes into water bodies. Additionally, the use of dyes in pharmaceuticals, cosmetics, and food processing further contributes to water pollution[7,8]. Improper disposal of dye-containing wastes and accidental spills during transportation and storage are also critical factors leading to the release of dyes into the aquatic environment. Organic dyes in water pose major environmental and human health risks. Environmentally, dyes can inhibit light penetration in water bodies, affecting photosynthetic activity and disrupting aquatic ecosystems. This can lead to reduced oxygen levels and the death of aquatic flora and

[1]Department of Chemistry, College of Science, Princess Nourah Bint Abdulrahman University, 11671 Riyadh, Saudi Arabia. [2]Chemistry Department, Faculty of Science, Benha University, Benha 13518, Egypt. [3]Department of Chemistry, Faculty of Science, Umm Al-Qura University, 21955 Makkah, Saudi Arabia. [4]Present address: Department of Chemistry, College of Science, Imam Mohammad Ibn Saud Islamic University (IMSIU), 11623 Riyadh, Saudi Arabia. ✉email: hesham.feky2010@yahoo.com; EAAAhmed@imamu.edu.sa

fauna. Dyes can also form toxic by-products through chemical reactions, further aggravating their environmental impact[9–11]. For humans, subjected to polluted water can induce several health difficulties. Some dyes are carcinogenic, mutagenic, and teratogenic, posing long-term health risks such as cancer and genetic mutations. Skin contact with dye-contaminated water can cause dermatitis and other skin disorders. Ingestion of contaminated water can induce gastrointestinal disturbances, liver and kidney damage, and other systemic effects[12–14]. Crystal violet dye, also known as gentian violet, is particularly hazardous to human health. It is extensively utilized in the textile and microbiological industries and has found purposes as a medicinal antiseptic. However, crystal violet is a potent mutagen and has been classified as a potential carcinogen. Chronic exposure can lead to severe health problems, including cancer, organ toxicity, and reproductive issues. Ingestion or prolonged skin contact can result in skin irritation, respiratory problems, and damage to vital organs such as the liver and kidneys[15,16]. Different approaches, such as adsorption[17,18], electrochemical [19], photocatalytic decomposition[20], as well as biological[21], have been designed to eliminate organic dyes from wastewater. Adsorption involves the accumulation of dye molecules on the surface of solid adsorbents. It is widely used owing to its simplicity, efficiency, and cost-effectiveness[22]. Common adsorbents include activated carbon, clay minerals, and metal oxides[23–25]. Electrochemical methods use electric current to degrade dye molecules. Techniques like electrocoagulation, electrooxidation, and electroflotation are employed to remove dyes from water. These methods are effective but can be energy-intensive and costly[26–28]. Photocatalytic degradation utilizes light-activated catalysts to break down dye molecules into less harmful substances. Titanium dioxide is a commonly used photocatalyst. This method is environmentally friendly but can be limited by the availability of suitable light sources[29]. The synthesis and application of novel materials offer significant advantages for environmental remediation, particularly in adsorption and photocatalysis processes[30–37]. Enhanced adsorption efficiency for heavy metals and organic pollutants, including Pb(II) ions, coupled with effective photocatalytic degradation of dyes such as eriochrome black T and trinitrophenol, has been demonstrated[38,39]. Biological methods involve the use of microorganisms to degrade dyes. Bacteria, fungi, and algae can metabolize dye molecules, converting them into non-toxic substances. While this approach is eco-friendly, it may require longer treatment times and specific environmental conditions[40–42]. The adsorption method offers several advantages over other dye removal techniques, such as efficiency, simplicity, cost-effectiveness, versatility, and environmental impact. Adsorption can effectively remove dyes at low concentrations and is capable of achieving high removal efficiencies. The process is straightforward and does not require complex equipment or highly skilled operators. Adsorbents are often inexpensive and can be regenerated and reused, reducing overall treatment costs[43]. Nano-metal oxides have gained prominence in adsorption due to their unique properties. Their high surface area, tunable pore sizes, and active surface sites enhance their sorption capacity and potency. Nano-metal oxides, for example, ZnO/MgO and $CaFe_2O_4$ exhibit excellent adsorption performance for a variety of organic dyes. Their ability to interact with dye molecules through various pathways, encompassing electrostatic attraction, van der Waals forces, and hydrogen bonding, makes them highly effective adsorbents[44,45]. Co_3O_4-based nanocomposites, such as Co/Co_3O_4, $ZnCo_2O_4/Co_3O_4$, and reduced graphene oxide/Co_3O_4, have demonstrated excellent adsorption and photocatalytic properties for various dyes in wastewater treatment applications[46–48]. Its high surface area, coupled with active surface sites, allows for efficient interactions with pollutants, making it a versatile adsorbent for environmental remediation[49]. No direct studies currently focus on the use of $Co_3(BO_3)_2$ for pollutant separation. However, research on similar borate compounds, such as magnesium borate ($Mg_3(BO_3)_2$), has shown promising results in adsorption applications. For instance, magnesium borate has demonstrated high efficiency in removing dyes from wastewater due to its structural properties and high surface area[50]. The Pechini sol–gel method is a versatile and efficient technique for synthesizing metal nanooxides. It involves the formation of a polymeric network through the reaction of metal salts with a chelating agent (typically citric acid) and a crosslinker (such as ethylene glycol). This method offers several advantages, such as control over composition and structure, uniform particle size, scalability, and versatility[51]. In this research, novel $Co_3O_4/Co_3(BO_3)_2$ nanostructures were synthesized using the Pechini sol–gel method with citric acid as a chelating agent and ethylene glycol as a crosslinker. The combination of cobalt oxide (Co_3O_4) and cobalt borate ($Co_3(BO_3)_2$) phases in a single material is unique, leveraging the synergistic effects of these components. This novel material composition is not extensively explored in previous research. This method's versatility and cost-effectiveness in producing high-performance adsorbents is a notable improvement over other approaches used in similar studies. The resulting nanostructures exhibit high surface area, uniform morphology, and enhanced adsorption properties towards crystal violet dye, making them suitable for water treatment applications. Also, the excellent reusability and minimal efficiency loss after multiple regeneration cycles position these nanostructures as more practical and cost-effective compared to many existing adsorbents, enhancing their significance for real-worldapplications.

Experimental

Materials

Ethylene glycol ($C_2H_6O_2$), Boric acid (H_3BO_3), cobalt nitrate hexahydrate ($Co(NO_3)_2{\cdot}6H_2O$), citric acid ($C_6H_8O_7$), hydrochloric acid (HCl), sodium hydroxide (NaOH), crystal violet dye ($C_{25}H_{30}ClN_3$), as well as potassium chloride (KCl) were bought from the Sigma-Aldrich Chemical Company. Each material was employed in its original form without any additional purification steps.

Synthesis of $Co_3O_4/Co_3(BO_3)_2$ nanostructures

$Co_3O_4/Co_3(BO_3)_2$ nanostructures were synthesized using the Pechini sol–gel method[50]. In this regard, 7.56 g of $Co(NO_3)_2{\cdot}6H_2O$ was solubilized in 70 mL of distilled water. Similarly, 1.51 g of H_3BO_3 was solubilized in another 70 mL of distilled water. Besides, the two aqueous solutions were then combined and stirred continuously for 5 min. Following this, citric acid solution, which was prepared by solubilizing 6.30 g of citric acid in 70 mL of

distilled water, was incorporated into the mixture under vigorous stirring for another 15 min. Next, 6 mL of ethylene glycol was added, and the blend was heated to 120 °C until total evaporation of the water was achieved. The resulting powder underwent calcination at 600 and 800 °C to produce $Co_3O_4/Co_3(BO_3)_2$ nanostructures, designated as EN600 and EN800, respectively. Figure 1 illustrates the synthesis process of $Co_3O_4/Co_3(BO_3)_2$ nanostructures. It is worth mentioning that the addition of 6.30 g of citric acid is based on the stoichiometric ratio required for chelation and complex formation in the Pechini sol–gel method. Citric acid serves as a chelating agent that binds to cobalt and borate ions, forming a stable metal-citrate complex. This chelation is crucial for ensuring homogeneity and controlled particle growth during the synthesis process.

Instrumentation

X-ray diffraction (XRD) patterns of the EN600 and EN800 samples were obtained using an X-ray diffractometer (D8 Discover, Bruker, USA). The Fourier transform infrared (FTIR) spectra of the EN600 and EN800 products were acquired utilizing an FTIR spectrometer (Nicolet IS10, Thermo Fisher Scientific, USA). The surface features of the EN600 and EN800 samples were investigated utilizing a field emission scanning electron microscope (FEG Quanta 250, FE-SEM, Thermo Fisher Scientific, USA). The particle morphology of the EN600 and EN800 samples was investigated utilizing a high-resolution transmission electron microscope (HRTEM, JEM-2100Plus, JEOL Ltd., Japan). The surface properties of the EN600 and EN800 products were acquired utilizing a nitrogen gas analyzer (NOVA2000 series, Quantachrome, USA). Energy dispersive X-ray (EDX) spectra of the EN600 and EN800 samples were obtained using a detector (X-Max 20, Oxford, England) attached to FE-SEM.

Removal of crystal violet dye from aquatic environments

The effectiveness of crystal violet dye removal was assessed in a dark place utilizing EN600 or EN800 adsorbents under various conditions, as outlined in Table 1. The experiments employed 100 mL solutions of crystal violet dye at a concentration of 150 mg/L, treated with 50 mg of the adsorbent. Adjusted variables included pH values between 2 and 10, contact times varying between 10 and 100 min, and temperatures varying between 298 and 328 K, as detailed in Table 1. Furthermore, the effects of crystal violet dye concentrations, between 50 and 250 mg/L, were evaluated while maintaining a constant solution volume as well as adsorbent dosage. The experimental procedure included stirring the crystal violet solutions for predetermined durations, separating the synthesized adsorbent through centrifugation, and subsequently calculating the remaining concentration of crystal violet dye at 590 nm utilizing an ultraviolet–visible (UV–Vis) spectrophotometer (Cintra 3030, GBC, Australia) to evaluate the adsorption performance.

Equations (1) and (2) were utilized to determine the adsorption capacity (O, mg/g) and removal efficiency (R %) of the synthesized adsorbents[52,53].

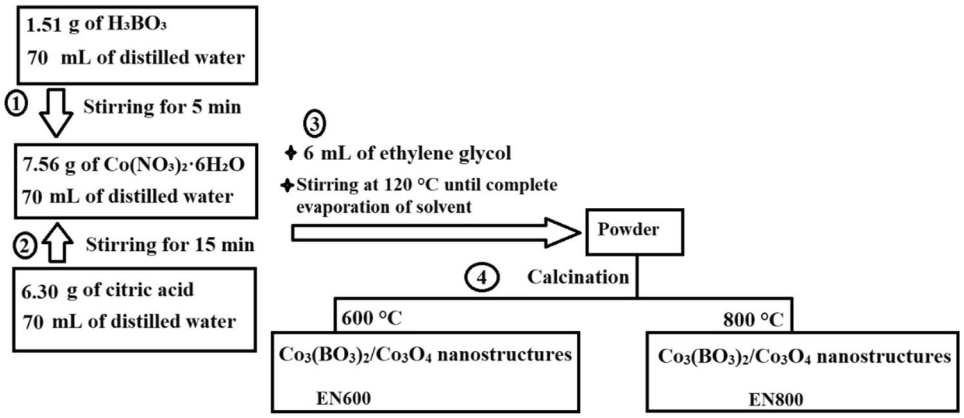

Fig. 1. Synthesis of $Co_3O_4/Co_3(BO_3)_2$ nanostructures.

Effect	Volume of studied dye solution (mL)	Concentration of studied dye (mg/L)	Amount of adsorbent (mg)	Temperature (K)	Time (min)	Solution pH
pH	100	150	50	298	360	2–10
Time	100	150	50	298	10–100	10
Temperature	100	150	50	298–328	70	10
Concentration of dye	100	50–250	50	298	70	10

Table 1. Experimental conditions for removing crystal violet dye from aquatic environments utilizing the EN600 and EN800 adsorbents.

$$O = (C_o - C_e) \times \frac{V}{W} z \quad (1)$$

$$R\,\% = \frac{C_o - C_e}{C_o} \times 100 \quad (2)$$

C_o indicates the preliminary concentration of crystal violet dye, expressed in mg/L. C_e indicates the residual concentration of crystal violet dye at equilibrium, also in mg/L. V refers to the volume of the crystal violet dye solution, measured in liters (L). W denotes the weight of the adsorbent used, measured in grams (g).

Elution was performed using hydrochloric acid (HCl) at 2, 4, and 6 M concentrations, with 50 mL of each concentration being used, to regenerate adsorbents saturated with crystal violet dye.

Equation (3) was employed to determine the desorption potential (D %) of crystal violet dye from the utilized adsorbent[54].

$$D\% = \frac{100 C_d V_d}{(C_o - C_e)V} \quad (3)$$

V_d indicates the desorptive solvent volume, measured in liters (L). C_d denotes the crystal violet dye concentration in the desorption solvent, expressed in mg/L.

Upon completion of regeneration, the durability and effectiveness of the utilized adsorbents were assessed over five successive cycles. In each cycle, 100 mL of a dye solution having a concentration of 150 mg/L was treated with an amount of 0.05 g of the adsorbent. Besides, the experimental settings, including a temperature of around 298 K, a contact time of 70 min, as well as a pH of 10, were consistently preserved throughout each cycle. After that, the adsorbent was separated by centrifugation, and then the remaining concentration of crystal violet dye was determined at 590 nm utilizing an ultraviolet–visible (UV–Vis) spectrophotometer.

Estimation of point of zero charge (pH_{PZC}) for the EN600 and EN800 products

To assess the pH_{PZC} for the EN600 and EN800 products, a batch procedure was implemented[55]. Initial pH measurements (pH_i) of 60 mL potassium chloride (KCl) solutions were set using 0.1 M NaOH or HCl and registered before the addition of 0.12 g of the synthesized adsorbent. Moreover, after 10 h of continuous mixing, the final pH measurements (pH_f) were registered. The differences between the initial and final pH points (ΔpH) were plotted with respect to the initial pH points. Furthermore, the point where the ΔpH against pH_i curve intersects the horizontal axis represents the pH_{PZC}.

Results and discussion

Production and identification of $Co_3O_4/Co_3(BO_3)_2$ nanostructures

The formation of $Co_3O_4/Co_3(BO_3)_2$ nanostructures via the Pechini sol–gel method involves a series of reactions that each play an essential role in the construction of the final product. Initially, cobalt nitrate hexahydrate undergoes dissociation to produce cobalt ions, as shown in Eq. (4).

$$Co(NO_3)_2 \cdot 6H_2O \rightarrow Co^{2+} + 2NO_3^- + 6H_2O \quad (4)$$

Following this, boric acid reacts with water to produce borate ions, which are vital for the next stages of synthesis, as shown in Eq. (5).

$$H_3BO_3 + H_2O \rightarrow B(OH)_4^- + H^+ \quad (5)$$

The cobalt ions then interact with the borate ions and citric acid to form a [CoB(Citrate)] complex, as demonstrated in Eq. (6).

$$Co^{2+} + B(OH)_4^- + C_6H_8O_7 \rightarrow [CoB(Citrate)]complex + 4H_2O \quad (6)$$

Ethylene glycol is subsequently introduced into the mixture, serving as an interlinking agent. Also, it undergoes a reaction with the carboxyl functional groups present in the citrate of the metal coordination complex, resulting in the establishment of ester bonds. This reaction leads to polymerization, producing a stable and viscous gel that effectively encapsulates the metal ions homogeneously within the framework. The resultant thick gel is then subjected to drying. This process eliminates water and initiates the solidification of the coordination complex. Finally, the polymeric network is subjected to heat, resulting in the formation of cobalt oxide and cobalt borate, alongside the evolution of carbon dioxide and water, as demonstrated in Eq. (7).

$$Polymericnetwork + heat \rightarrow Co_3(BO_3)_2 + Co_3O_4 + CO_2 + H_2O \quad (7)$$

XRD analysis was utilized to investigate the structural properties of the EN600 and EN800 products, as demonstrated in Fig. 2A,B, respectively. Both samples contain two distinct crystalline phases: Co_3O_4 (82.91%), which crystallizes in a cubic system, and $Co_3(BO_3)_2$ (17.10%), which crystallizes in an orthorhombic system. These phases are confirmed by their respective JCPDS files, with Co_3O_4 being linked to JCPDS No. 00-009-0418 and $Co_3(BO_3)_2$ to JCPDS No. 00-025-0102. The characteristic peaks at $2\Theta^o$ (hkl) values of 33.32° (121), 40.03° (211), 42.33° (102), 52.33° (202), 54.63° (132), 60.50° (330), 61.41° (142), and 68.58° (251), indicate the orthorhombic structure of $Co_3(BO_3)_2$. The characteristic peaks at $2\Theta^o$ (hkl) values of 19.01° (111), 31.29° (220), 36.82° (311), 38.56° (222), 44.79° (400), 55.73° (422), 59.40° (511), and 65.28° (440), indicate the cubic structure of Co_3O_4. The

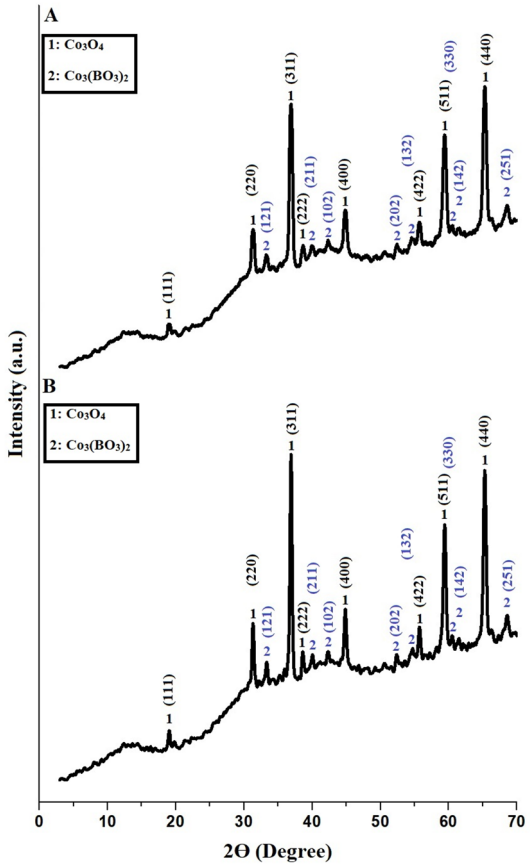

Fig. 2. XRD patterns of the EN600 (**A**) and EN800 (**B**) products.

average crystal size of the EN600 sample is 43.82 nm, while the EN800 sample exhibits a larger average crystal size of 52.93 nm. This increase in average crystal size can be attributed to the higher temperature, which promotes the formation of larger crystals. These values are comparable to those reported for other cobalt-based nanocomposites, such as $ZnCo_2O_4/Co_3O_4$ (40–60 nm) synthesized by Heidari-Asil et al., where higher temperatures similarly resulted in increased crystal sizes[47]. Additionally, the crystal structure comparison aligns with findings from other borate compounds like magnesium borate ($Mg_3(BO_3)_2$), which exhibit similar crystalline behavior[50].

Table 2 tabulates the surface characteristics of both samples. Also, the N_2 adsorption/desorption isotherms for both samples, as depicted in Fig. 3, exhibit a type IV isotherm with a noticeable H3 hysteresis loop, characteristic of mesoporous materials[50]. The isotherm curves reveal that the EN600 sample adsorbs more N_2 at higher relative pressures compared to the EN800, aligning with its larger pore volume and surface area, as shown in Table 2. The BET surface area and total pore volume are higher for the EN600 sample compared to the EN800 sample. This suggests that the EN600 sample possesses a more porous structure, potentially facilitating enhanced N_2 adsorption capabilities. The average pore sizes of the EN600 and EN800 samples are relatively similar, with values of 8.12 and 8.38 nm, respectively. Despite the minor difference in average pore size, this similarity implies that the overall porosity characteristics of the samples are comparable in terms of the size of the pores, although the total number and volume of these pores differ. The BET surface area for EN600 (65.80 m^2/g) is significantly higher than that of EN800 (43.76 m^2/g), which corresponds to their enhanced adsorption capabilities. These values are notably larger than those reported for other nanocomposites, such as $Mn_{0.5}Zn_{0.5}Fe_2O_4/Fe_2O_3$ (43.18 m^2/g), copper oxide/cobalt manganese oxide/manganese oxide (33.37 m^2/g), and MgO/Cu_3MgO_4 (42.20 m^2/g)[56–58].

Surface textures	EN600	EN800
Total pore volume (cc/g)	0.2672	0.1834
BET surface area (m^2/g)	65.80	43.76
Average pore size (nm)	8.12	8.38
Isotherm type	Type IV	Type IV
Hysteresis loop type	Type H3	Type H3

Table 2. BET surface textures of the EN600 and EN800 products.

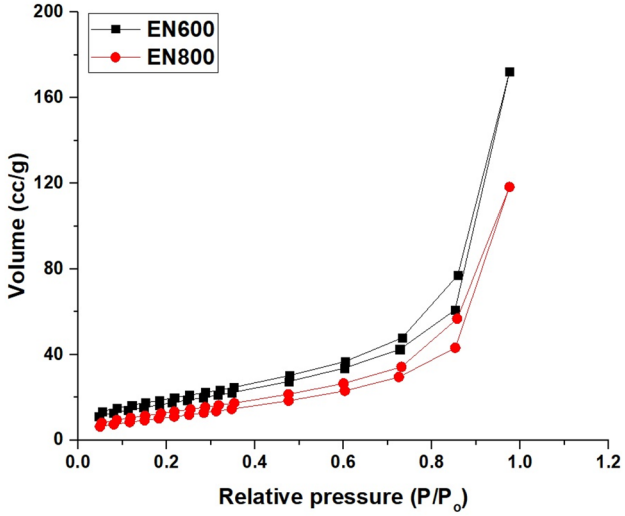

Fig. 3. N_2 adsorption/desorption isotherms of the EN600 and EN800 products.

FE-SEM analysis was conducted on the EN600 and EN800 products, as depicted in Fig. 4A,B, respectively. In the images, variations in the surface morphology and grain sizes of the two samples are clearly observed. The average grain size for the EN600 sample is 0.23 µm, where a denser and more uniform distribution of smaller grains is evident. Conversely, a larger average grain size of 0.34 µm is noted in the EN800 sample, along with a less uniform distribution of grains, indicating a coarser structure. These morphological properties are almost similar to those observed in several nanocomposites, such as ZnO/MgO composite (average grain size ~ 0.37 µm),

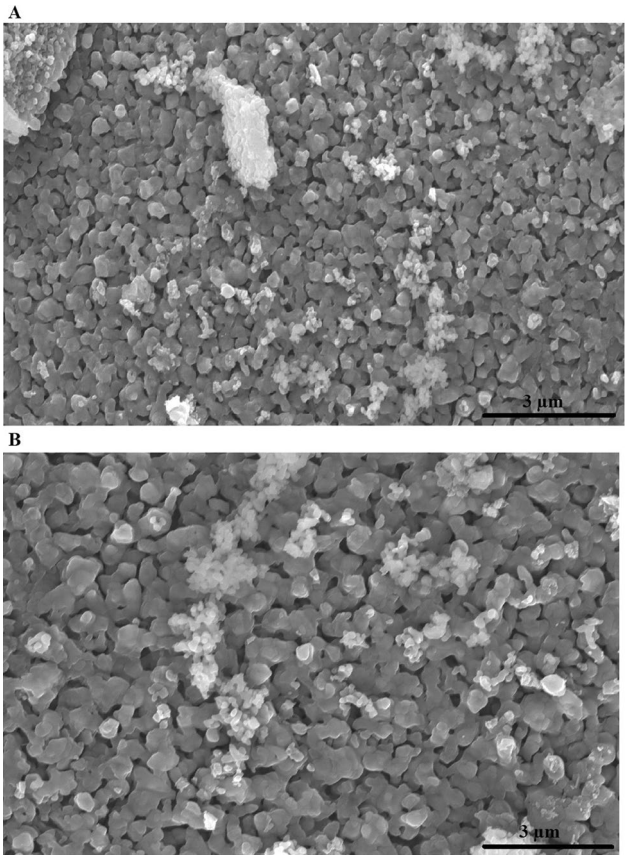

Fig. 4. FE-SEM images of the EN600 (**A**) and EN800 (**B**) products.

$Mn_{0.5}Zn_{0.5}Fe_2O_4/Fe_2O_3$ (average grain size ~ 0.47 µm), and copper oxide/cobalt manganese oxide/manganese oxide (average grain size ~ 0.42 µm) which are known for their high adsorption efficiency due to similar structural attributes[44,57,59]. The smaller grain size and denser distribution in EN600 likely lead to more available active sites for adsorption, which directly enhances its efficiency in dye removal compared to EN800. This structural difference aligns with the observed higher BET surface area and adsorption capacity of EN600.

HR-TEM analysis was conducted on the EN600 and EN800 samples, as outlined in Fig. 5A,B, respectively. The EN600 sample displayed an average particle diameter of 102.84 nm, where the particles appear somewhat agglomerated. Conversely, the EN800 sample has a larger average diameter of 148.89 nm, which is indicative of significant coalescence among particles. The difference in particle sizes between the EN600 (102.84 nm) and EN800 (148.89 nm) samples, can be attributed to the increased calcination temperature for EN800, which leads to greater particle growth and agglomeration. The higher calcination temperature of 800 °C enhances atomic diffusion and crystal growth, resulting in larger particle sizes due to the sintering effect. This behavior is consistent with findings reported in the literature for similar nanostructures, such as $ZrO_2/MgMn_2O_4/Mg(Mg_{0.333}Mn_{1.333})O_4$, barium titanate, and $ZrO_2/CdMn_2O_4/CdO$[60–62]. The larger particle size in EN800 reduces its surface area, negatively impacting its adsorption efficiency compared to EN600. It is noted that the observed differences in particle sizes between the HR-TEM and XRD analyses are attributed to the tendency of the samples to coalesce. This coalescence leads to larger apparent sizes in the HR-TEM images compared to the crystallite sizes determined by XRD, which typically measures the size of coherent scattering regions within the crystals.

Figure 6A,B represents the FTIR absorption spectra of the EN600 and EN800 products, respectively. Besides, the stretching vibration modes associated with Co(III)-O in an octahedral coordination and Co(II)-O in a tetrahedral coordination within Co_3O_4 were recorded at 581 and 676 cm^{-1} for EN600 and 553 and 638 cm^{-1} for EN800, respectively[63]. Moreover, the B-O-B bending vibrations were noted at 883 cm^{-1} for EN600 and 869 cm^{-1} for EN800. The B-O-B symmetric stretching vibration modes showed at 1181 cm^{-1} for EN600 and 1163 cm^{-1} for EN800. The B-O-B asymmetric stretching vibrations appeared at 1285 cm^{-1} for EN600 and 1257 cm^{-1} for

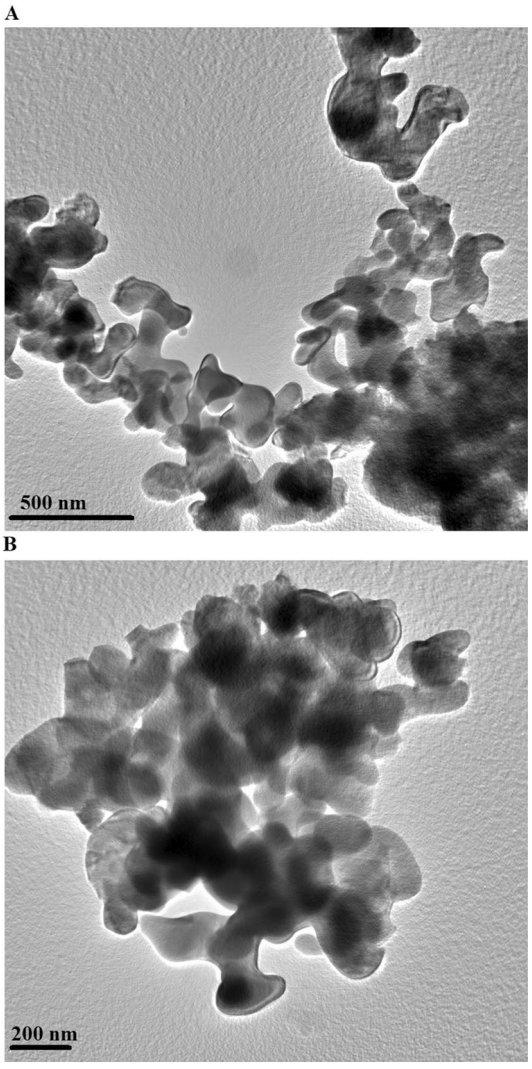

Fig. 5. HR-TEM images of the EN600 (**A**) and EN800 (**B**) products.

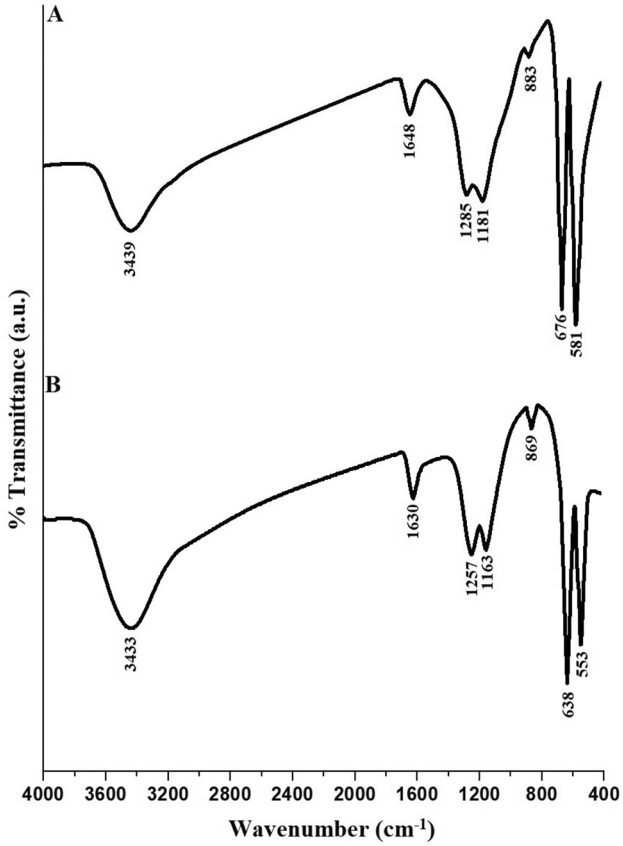

Fig. 6. FTIR Spectra of the EN600 (**A**) and EN800 (**B**) products.

EN800[64,65]. Bending vibration modes from adsorbed water were identified at 1648 cm^{-1} for EN600 and 1630 cm^{-1} for EN800. Additionally, the stretching vibration modes of adsorbed water were recorded at 3439 cm^{-1} for EN600 and 3433 cm^{-1} for EN800[66]. The FTIR spectra for EN600 and EN800 products are discussed, showing vibration modes associated with Co(III)-O and Co(II)-O bonds and the specific B-O-B bending and stretching vibrations that confirm the presence of $Co_3(BO_3)_2$. The peak positions (e.g., 581 and 676 cm^{-1} for EN600 and 553 and 638 cm^{-1} for EN800) are detailed, explaining how these correspond to the nanostructures identified through XRD.

The elemental composition of the EN600 and EN800 nanostructures was determined through energy dispersive X-ray (EDX) analysis, as illustrated in Fig. 7A,B, respectively. The EDX spectra, as shown in Table 3, confirm the presence of cobalt (Co), oxygen (O), and boron (B) elements, aligning with the expected composition of the $Co_3(BO_3)_2/Co_3O_4$ composite.

Removal of crystal violet dye from aquatic environments

Influence of dye solution pH

In the analysis presented in Fig. 8A, the influence of solution pH on the elimination percentage of crystal violet dye applying the EN600 and EN800 adsorbents was systematically examined. The disposal percentage of the crystal violet dye was observed to increase with rising pH values for both samples. The highest removal percentage was observed at pH 10, with EN600 achieving 93.17% and EN800 achieving 82.91%.

The relationship between pH and adsorption efficacy is closely linked to the point of zero charge (pH_{PZC}) of the adsorbents, which was detected to be 6.75 for EN600 and 7.28 for EN800, as shown in Fig. 8B. The point of zero charge is critical, as it indicates the pH at which the surface charge of the adsorbent is neutral. Below the pH_{PZC}, the surface of the adsorbents is positively charged, enhancing electrostatic repulsion with the positively charged crystal violet dye molecules, thus explaining the decreased dye removal efficiency as shown in Fig. 9[67]. Above the pH_{PZC}, the surface of the adsorbents becomes negatively charged, enhancing electrostatic attraction with the positively charged crystal violet dye molecules and thus explaining the increased crystal violet removal efficiency as indicated in Fig. 9[68].

Influence of contact time

Figure 10 exhibits the systematic study of crystal violet dye removal using EN600 and EN800 adsorbents at different times. An increasing trend in the percentage of crystal violet dye removal was observed from 10 to 70 min for both samples. The highest removal percentage was observed at 70 min, with EN600 achieving 92.45%

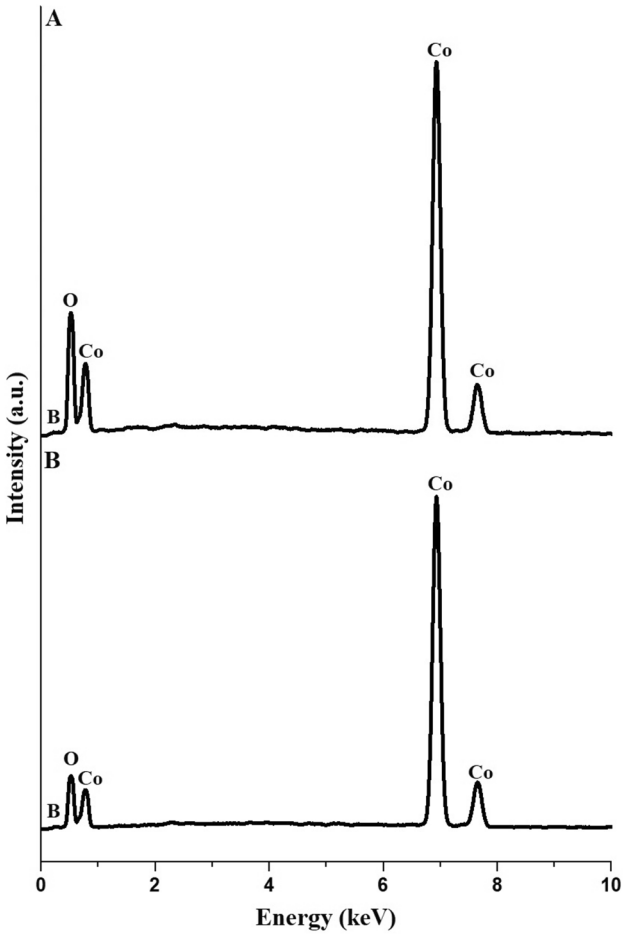

Fig. 7. EDX patterns of the EN600 (**A**) and EN800 (**B**) products by EDX.

Samples	Weight percentage		
	Co	O	B
EN600	68.10	30.20	1.70
EN800	70.24	28.23	1.53

Table 3. Elemental composition of the EN600 and EN800 products.

and EN800 achieving 82.38%. Beyond 70 min, both adsorbents reached a plateau in crystal violet dye removal efficiency owing to the saturation of active sites[69].

The findings were analyzed with the application of pseudo-second-order in addition to the pseudo-first-order kinetic models, as depicted in Eqs. (8) and (9), respectively[52,53].

$$\frac{t}{O_t} = \frac{1}{F_2 O_e^2} + \frac{1}{O_e} t \tag{8}$$

$$\log(O_e - O_t) = \log O_e - \frac{F_1}{2.303} t \tag{9}$$

Measured in mg/g, O_t and O_e indicate the amount of crystal violet dye separated at contact time t in addition to at equilibrium, respectively.

Furthermore, F_1 and F_2 are the rate constants for the pseudo-first-order in addition to the pseudo-second-order models, respectively, quantified in 1/min and g/mg min. Figure 11A,B display the utilization of both pseudo-second-order and pseudo-first-order models in the adsorption of crystal violet dye utilizing EN600 and EN800 adsorbents, respectively. Table 4 lists the kinetic parameters associated with the discarding of crystal violet dye using these adsorbents. The evaluation of the kinetic findings reveals that the pseudo-second-order provides a more precise fit than the pseudo-first-order, as corroborated by the greater R^2 values of 0.9999 for

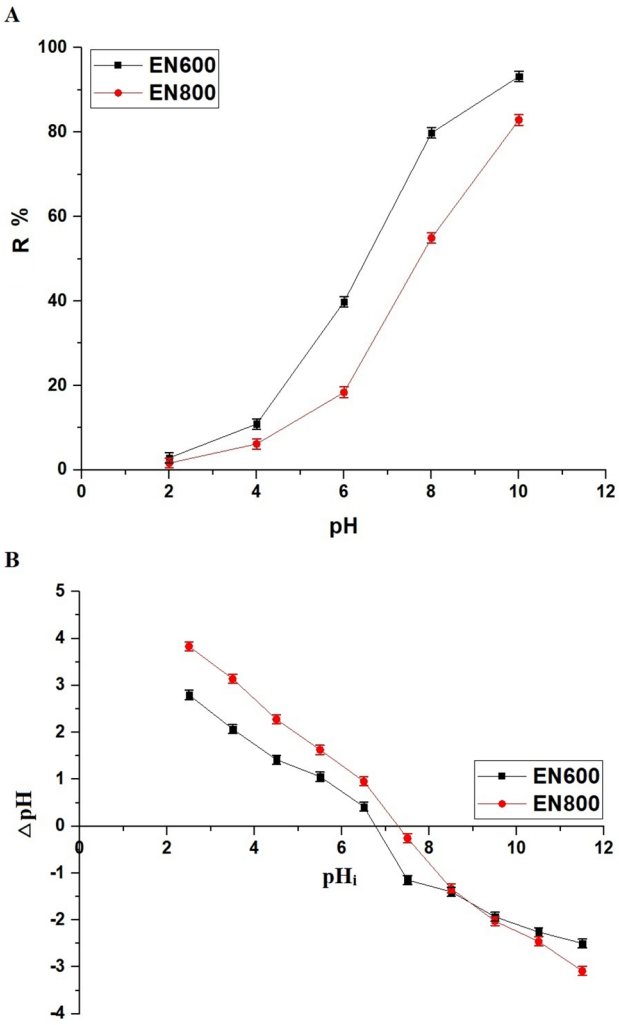

Fig. 8. (**A**) Correlation between primarily pH values and the elimination percentage of crystal violet dye by EN600 and EN800 adsorbents. (**B**) Measurement of pH_{PZC} for the EN600 as well as EN800 products.

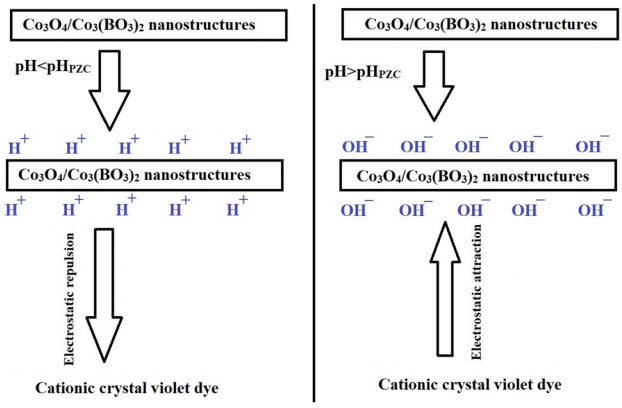

Fig. 9. The mechanism of adsorption of crystal violet dye using $Co_3O_4/Co_3(BO_3)_2$ nanostructures.

EN600 in addition to 0.9997 for EN800 in the pseudo-second-order, in contrast to 0.9612 as well as 0.9767 in the pseudo-first-order for the same materials, respectively. Additionally, the close match between the O_e values and O_{EXP} in the pseudo-second-order reveals that the discarding of crystal violet dye onto the EN600 and EN800 products predominantly adheres to this model. Moreover, the rate constants for EN600 (0.000355 g/mg min)

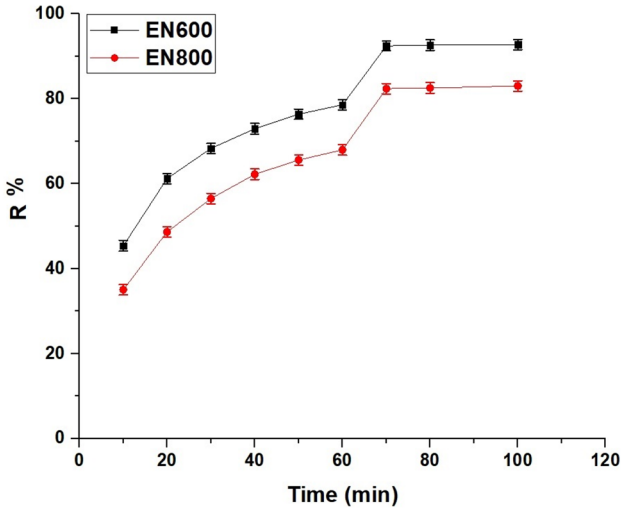

Fig. 10. Correlation between contact time and the percentage of crystal violet dye removed by EN600 and EN800 adsorbents.

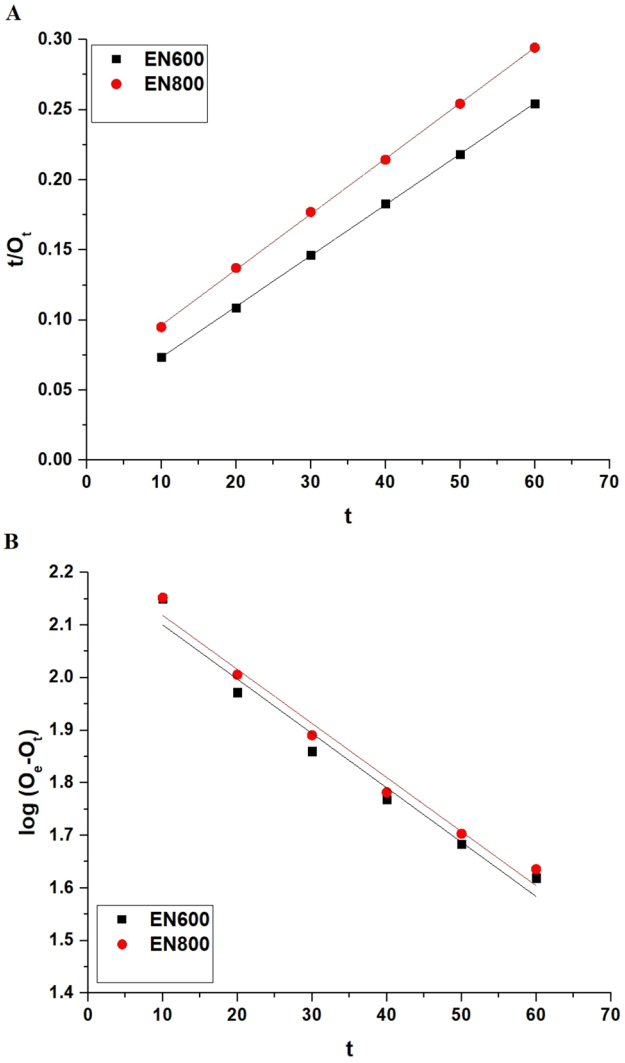

Fig. 11. The pseudo-second-order (**A**) in addition to the pseudo-first-order (**B**) kinetic models for disposing of crystal violet dye by EN600 and EN800 products.

Adsorbent	O_{Exp} (mg/g)	Pseudo-first-order			Pseudo-second-order		
		F_1 (1/min)	R^2	O_e (mg/g)	F_2 (g/mg.min)	R^2	O_e (mg/g)
EN600	277.36	0.0238	0.9612	159.80	0.000355	0.9999	275.48
EN800	247.14	0.0237	0.9767	166.41	0.000276	0.9997	252.53

Table 4. Kinetic constants for crystal violet dye removal by EN600 and EN800 adsorbents.

and EN800 (0.000276 g/mg min) align with those reported for metal oxide adsorbents like ZnO/MgO and ZrO_2/$CdMn_2O_4$/CdO composites[44,61].

Effect of temperature

The effectiveness of the EN600 and EN800 adsorbents in removing crystal violet dye at different temperatures was assessed, as depicted in Fig. 12A. Both adsorbents demonstrated a consistent decrease in the percentage of crystal violet dye removal as the solution temperature elevated from 298 K up to 328 K.

Equations (10), (11), and (12) were employed to calculate the Gibbs free energy (ΔG°), entropy change (ΔS°), as well as enthalpy change (ΔH°) for the discarding of crystal violet dye utilizing the EN600 and EN800 products[58]

$$\ln F_d = \frac{\Delta S^\circ}{R} - \frac{\Delta H^\circ}{RT} \tag{10}$$

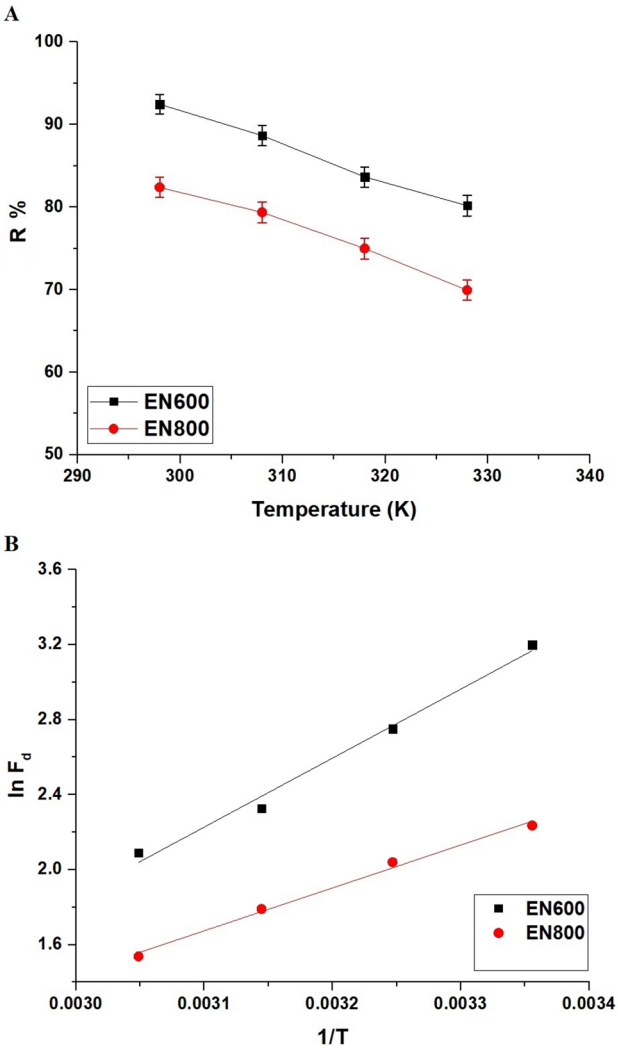

Fig. 12. (**A**) Correlation between temperature and the percentage of crystal violet dye removed by EN600 and EN800 adsorbents. (**B**) The graph of ln F_d against 1/T.

$$\Delta G^{\circ} = \Delta H^{\circ} - T\Delta S^{\circ} \tag{11}$$

$$F_d = \frac{O_e}{C_e} \tag{12}$$

F_d, T, and R symbolize the distribution coefficient, temperature, and gas constant, respectively, measured in units of L/g, K, and kJ/molK. Figure 12B illustrates the graph of ln F_d vs. 1/T for the discarding of studied crystal violet dye by the EN600 and EN800 products. Table 5 details the previous thermodynamic constants for the adsorption operation using these adsorbents. The positive alteration in entropy ($\Delta S > 0$) suggests that the disposal of crystal violet dye onto the EN600 or EN800 adsorbents is feasible, marked by a growth in irregularity at the liquid–solid boundary. An alteration in enthalpy (ΔH) fewer than 40 kJ/mol indicates that the elimination mechanism is principally physical. The negative enthalpy change ($\Delta H < 0$) demonstrates the exothermic nature of the adsorption process. A negative Gibbs free energy change ($\Delta G < 0$) indicates that the disposal of crystal violet dye is a spontaneous process. These findings regarding thermodynamic parameters are consistent with those reported in similar composites, such as ZnO/MgO and $ZrO_2/CdMn_2O_4/CdO$[44,61].

Effect of concentration

The removal efficiency of crystal violet dye from aqueous solutions using EN600 and EN800 adsorbents decreases as the initial concentration of the crystal violet dye elevates, as revealed in Fig. 13. This trend may be assigned to the fullness of the provided adsorption positions on the adsorbents. At lower crystal violet dye concentrations, there are more accessible active centers relative to the number of crystal violet dye particles, leading to greater removal efficiency. Nevertheless, as the crystal violet dye concentration increases, the available adsorption positions become saturated, and the removal efficiency per unit mass of adsorbent decreases. This is because the adsorbents reach their maximum capacity, while the excess dye molecules remain in the solution.

The experimental results for the disposal of crystal violet dye on EN600 and EN800 adsorbents were evaluated using both the Langmuir (Eq. 13) and Freundlich (Eq. 14) isotherms[52,53].

$$\frac{C_e}{O_e} = \frac{1}{F_3 O_{max}} + \frac{C_e}{O_{max}} \tag{13}$$

$$\ln O_e = \ln F_4 + \frac{1}{n} \ln C_e \tag{14}$$

Adsorbent	ΔS° (kJ/molK)	ΔH° (kJ/mol)	ΔG° (kJ/mol)			
			298	308	318	328
EN600	0.0767	− 30.74	− 53.58	− 54.35	− 55.12	− 55.88
EN800	0.0452	− 19.10	− 32.58	− 33.03	− 33.48	− 33.93

Table 5. Thermodynamic parameters for crystal violet dye removal using the EN600 and EN800 products.

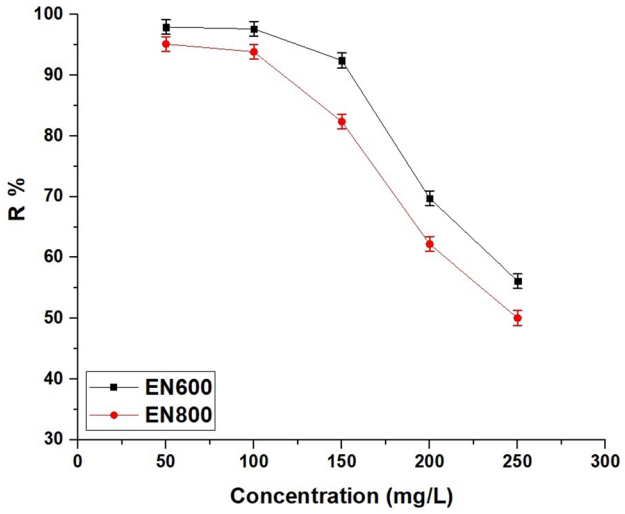

Fig. 13. Correlation between preliminary concentration of dye and the percentage of crystal violet dye removed by EN600 and EN800 adsorbents.

where, C_e operates as the equilibrium concentration of the crystal violet dye (mg/L), O_e operates as the amount of crystal violet dye adsorbed per unit mass of adsorbent (mg/g), O_{max} operates as the maximum adsorption capacity (mg/g), F_3 is the Langmuir constant (L/mg), F_4 is the Freundlich constant (mg/g) $(L/mg)^{1/n}$), and n is the heterogeneity factor. Equation (15) represents the calculation of O_{max} from the Freundlich equilibrium isotherm[70].

$$O_{max} = F_4\left(C_o^{1/n}\right) \tag{15}$$

The uptake behavior of crystal violet dye on EN600 and EN800 adsorbents was investigated through the Langmuir and Freundlich isotherms, as illustrated in Fig. 14A,B and detailed in Table 6. The adsorption process does not follow the Freundlich isotherm, as indicated by the lower correlation coefficients (R^2) of 0.6076 for EN600 and 0.6741 for EN800. The Langmuir isotherm, which assumes monolayer adsorption on a surface with a finite number of identical sites, fits the experimental results exceptionally well, as indicated by the high correlation coefficients (R^2) of 0.9998 for EN600 and 0.9994 for EN800. The maximum adsorption capacity (O_{max}) obtained from the Langmuir model is 284.09 mg/g for EN600 and 256.41 mg/g for EN800. This suggests that EN600 has a

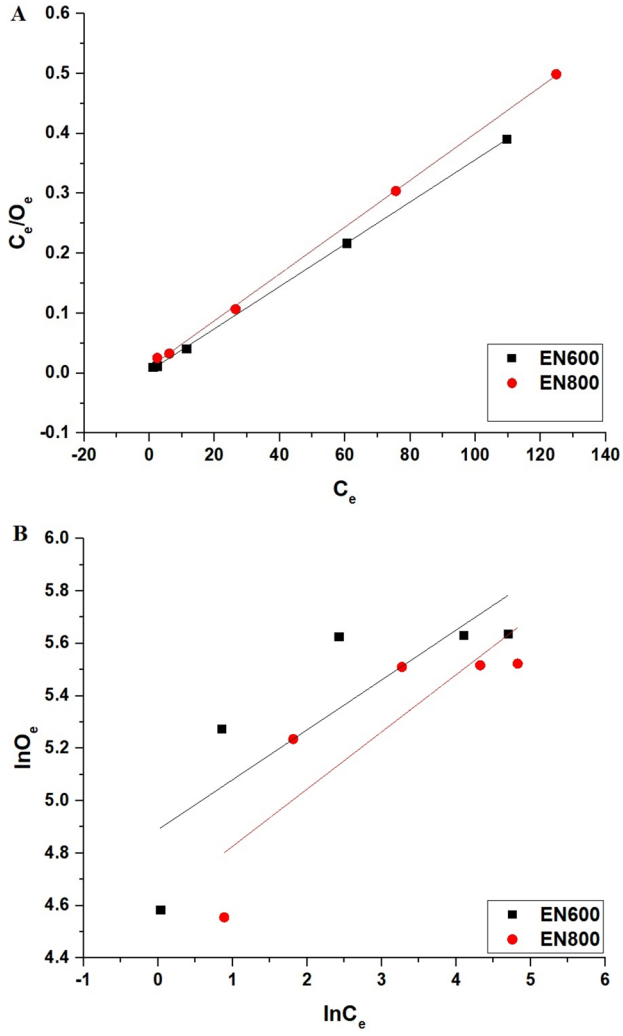

Fig. 14. Langmuir (**A**) in addition to Freundlich (**B**) graphs for the adsorption of crystal violet dye by EN600 and EN800 products.

Adsorbent	Langmuir			Freundlich			
	O_{max} (mg/g)	R^2	F_3 (L/mg)	F_4 (mg/g)$(L/mg)^{1/n}$	O_{max} (mg/g)	1/n	R^2
EN600	284.09	0.9998	0.8980	132.94	344.72	0.1902	0.6076
EN800	256.41	0.9994	0.3971	100.30	299.03	0.2180	0.6741

Table 6. Langmuir and Freundlich isotherm parameters for EN600 and EN800 products.

slightly higher capacity for crystal violet dye removal compared to EN800, possibly due to differences in surface properties or pore structure. Moreover, these findings regarding equilibrium constants are consistent with those reported in similar composites, such as ZnO/MgO and ZrO_2/$CdMn_2O_4$/CdO[44,61].

This study compared the elimination capacity of multiple adsorbents for crystal violet dye, as outlined in Table 7[71–79]. EN600 exhibited the highest capacity at 284.09 mg/g, followed by EN800 at 256.41 mg/g, both significantly outperforming other adsorbents. The exceptional performance of recently established EN600 and EN800 products demonstrates their viability for enhanced crystal violet dye removal from effluents. These observations emphasize developments in adsorption procedures and the crucial significance of matter engineering in environmental decontamination. The crystal size plays a crucial role in determining the surface area and the availability of active sites for adsorption. The smaller nanoparticle size in EN600 (43.82 nm) corresponds to a higher BET surface area (65.80 m^2/g) compared to EN800 (52.93 nm, 43.76 m^2/g). This difference is a critical factor influencing the adsorption capacity, with EN600 showing a higher maximum adsorption capacity of 284.09 mg/g for crystal violet dye, compared to 256.41 mg/g for EN800. This finding is consistent with literature, where smaller nanoparticle sizes typically lead to higher adsorption efficiencies due to the increased surface area and better dispersion of nanoparticles within the solution.

Assessment of regeneration and reusability

This research evaluated the impact of different HCl concentrations on the discarding of crystal violet dye from EN600 and EN800 adsorbents, as shown in Fig. 15. The findings revealed that increasing HCl concentrations enhanced crystal violet dye removal efficiency for both adsorbent types. At a 6 M concentration, desorption efficiencies were 99.86% for EN600 and 99.93% for EN800. These results indicate a strong correlation between desorption efficiency and the acidity level of the eluent. Higher HCl concentrations likely improve desorption percentages by breaking the bonds between crystal violet dye particles and adsorbent surfaces. Besides, the nearly

Adsorbent	O_{max} (mg/g)	References
Polypyrrole-decorated bentonite magnetic composite	78.74	[71]
Poly(acrylamide)-Kaolin	25.00	[72]
Natural zeolite	177.75	[73]
Magnetic g-poly(methacrylic acid)-κ-carrageenan	28.24	[74]
Fe_3O_4/sodium dodecyl sulphate composite	166.70	[75]
Silica aerogel	137.17	[76]
Silver/graphene oxide composite	48.78	[77]
Activated carbon/Fe_3O_4 composite	35.30	[78]
Calcium oxide modified fly ash	32.12	[79]
EN600	284.09	This study
EN800	256.41	This study

Table 7. Evaluation of maximum elimination capacities for different adsorbents concerning crystal violet dye.

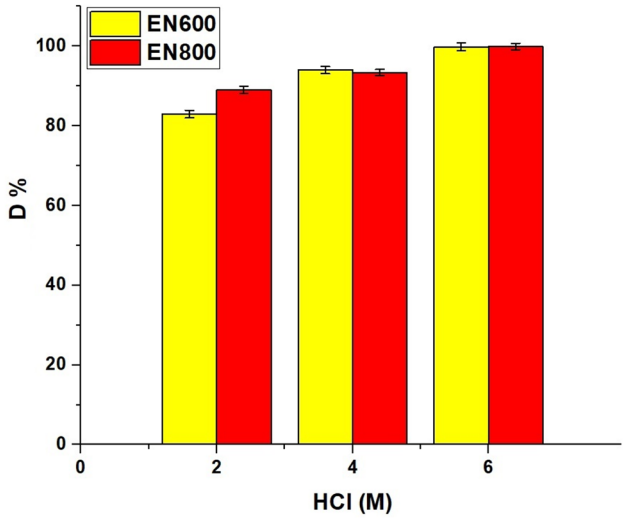

Fig. 15. Efficiency of crystal violet dye desorption from EN600 and EN800 adsorbents at varying HCl concentrations.

whole crystal violet dye removal at this concentration emphasizes the feasibility of reactivating and reusing the adsorbents. The research highlights the necessity of optimizing the eluent concentration to maximize crystal violet dye recovery and promote the sustainable use of adsorbents. It also demonstrates that both EN600 and EN800 adsorbents are highly effective for repeated use with strong desorption performance.

The repeated application of EN600 and EN800 products for the extraction of crystal violet dye was comprehensively tested across multiple cycles, as illustrated in Fig. 16. The crystal violet dye removal efficiency demonstrated stable behavior throughout the five cycles, implying that the adsorbents maintained their performance despite repeated use. This stable performance across multiple cycles underscores the economic feasibility and prolonged effectiveness of these products in water purification processes.

The structural stability of the EN600 and EN800 adsorbents after multiple adsorption–desorption cycles was thoroughly analyzed using XRD (Figures omitted for brevity). The XRD patterns of the reused EN600 and EN800 samples indicate that the crystalline phases of Co_3O_4 and $Co_3(BO_3)_2$ remain stable after repeated cycles. The characteristic peaks for both phases are still present, with only very slight broadening observed, which is attributed to minor changes in crystallite size due to potential surface restructuring during the adsorption–desorption processes[80].

Practical application

In a practical demonstration of the utility of $Co_3O_4/Co_3(BO_3)_2$ nanostructures, experiments were conducted to assess the adsorption performance of the EN600 and EN800 samples in a student chemistry laboratory wastewater (containing crystal violet dye). For these experiments, 0.05 g of each adsorbent type was introduced into 100 mL of wastewater sample containing crystal violet dye at a concentration of 60 mg/L. The pH of the solution was adjusted to 10, and the system was maintained at room temperature for a contact time of 70 min to simulate typical laboratory conditions. The EN600 sample achieved a crystal violet dye removal efficiency of 97.52%, while the EN800 sample demonstrated an enhanced removal efficiency of 93.29%. This significant efficacy in crystal violet dye removal underscores the potential of $Co_3O_4/Co_3(BO_3)_2$ nanostructures, particularly the EN600 type, for application in the wastewater treatment field.

Conclusions

In this work, novel $Co_3O_4/Co_3(BO_3)_2$ nanostructures were synthesized via a simple Pechini sol–gel method, representing a unique combination of cobalt oxide and cobalt borate phases tailored for enhanced crystal violet dye adsorption. These nanostructures, which were synthesized at 600 and 800 °C, were abbreviated as EN600 and EN800, respectively. The mean crystal sizes were 43.82 nm for EN600 and 52.93 nm for EN800. The BET surface areas were 65.80 m^2/g for EN600 and 43.76 m^2/g for EN800, respectively. Optimal removal of crystal violet dye was achieved at a solution temperature of 298 K, an interaction time of 70 min, and a pH of 10. The synthesized EN600 and EN800 nanostructures demonstrate exceptionally high adsorption capacities of 284.09 mg/g and 256.41 mg/g for crystal violet dye, respectively, outperforming many conventional adsorbents. The innovation of this research lies in the development of a dual-phase material that leverages the synergistic effects of cobalt oxide's high reactivity and cobalt borate's structural stability. This novel material composition, combined with a scalable and cost-effective synthesis approach, provides a new avenue for sustainable environmental remediation. The adsorption process, which aligns best with the pseudo-second-order model and Langmuir isotherm, was determined to be exothermic, physical, and spontaneous. Besides, the adsorbents were effectively regenerated with 6 M hydrochloric acid and reused several times with minimal efficiency loss, demonstrating their excellent

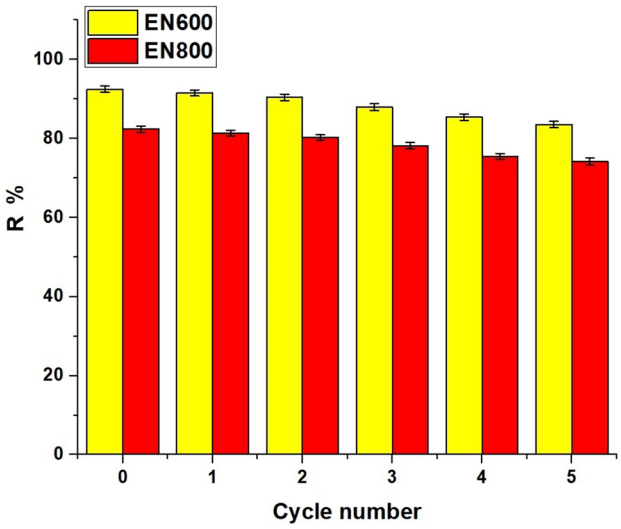

Fig. 16. Reusability of EN600 and EN800 products across multiple cycles for crystal violet dye adsorption.

reusability. Future research will focus on scaling up the synthesis of EN600 and EN800 nanostructures for larger-scale environmental remediation applications.

Data availability

All data generated or analyzed during this study are included in this published article.

Received: 2 August 2024; Accepted: 2 September 2024
Published online: 16 September 2024

References

1. Anulaya, S. V., Subash, A., Gholap, V. & Kandasubramanian, B. Electrospinning of cellulose acetate for methylene blue dye removal. *Hybrid Adv.* **6**, 100205 (2024).
2. Park, D. *et al.* Removal of selected contaminants of dyes and pharmaceuticals using MXene-based nanoadsorbents: A review. *Sep. Purif. Technol.* **341**, 126864 (2024).
3. Gadore, V., Mishra, S. R., Yadav, N., Yadav, G. & Ahmaruzzaman, M. Advances in zeolite-based materials for dye removal: Current trends and future prospects. *Inorg. Chem. Commun.* **166**, 112606 (2024).
4. Xu, D. *et al.* Efficient recycling of sewage water in a polyester integrated industry: A case study. *Desalin. Water Treat.* **319**, 100508 (2024).
5. Kausar, A. *et al.* Cellulose-based materials and their adsorptive removal efficiency for dyes: A review. *Int. J. Biol. Macromol.* **224**, 1337–1355 (2023).
6. Athab, Z. H. *et al.* Comparison activity of pure and chromium-doped nickel oxide nanoparticles for the selective removal of dyes from water. *Sci. Rep.* **14**, 1–15 (2024).
7. Zhao, Z., Li, L., Geleta, G. S., Ma, L. & Wang, Z. Polyacrylamide-phytic acid-polydopamine conducting porous hydrogel for efficient removal of water-soluble dyes. *Sci. Rep.* **7**, 1–10 (2017).
8. Liu, D., Lei, W., Qin, S. & Chen, Y. Template-free synthesis of functional 3D BN architecture for removal of dyes from water. *Sci. Rep.* **4**, 1–5 (2014).
9. Ahmadian, M., Derakhshankhah, H. & Jaymand, M. Biosorptive removal of organic dyes using natural gums-based materials: A comprehensive review. *J. Ind. Eng. Chem.* **124**, 102–131 (2023).
10. Jiao, T. *et al.* Facile and scalable preparation of graphene oxide-based magnetic hybrids for fast and highly efficient removal of organic dyes. *Sci. Rep.* **5**, 1–10 (2015).
11. Zhao, X. *et al.* Synthesis of magnetic metal-organic framework (MOF) for efficient removal of organic dyes from water. *Sci. Rep.* **5**, 1–10 (2015).
12. Aouaini, F. *et al.* Statistical physics analysis of the adsorption of reactive red 141dye on residual avocado peel (*Persea americana*) chemically modified with H2SO4 and HNO3. *Inorg. Chem. Commun.* **165**, 112547 (2024).
13. Kamaraj, M. *et al.* β-cyclodextrin polymer composites for the removal of pharmaceutical substances, endocrine disruptor chemicals, and dyes from aqueous solution—A review of recent trends. *J. Environ. Manag.* **351**, 119830 (2024).
14. Elzahar, M. M. H. & Bassyouni, M. Removal of direct dyes from wastewater using chitosan and polyacrylamide blends. *Sci. Rep.* **13**, 1–16 (2023).
15. Al-Ansari, S. H., Gomaa, H., Abdel-Rahim, R. D., Ali, G. A. M. & Nagiub, A. M. Recycled gold-reduced graphene oxide nanocomposite for efficient adsorption and photocatalytic degradation of crystal violet. *Sci. Rep.* **14**, 1–16 (2024).
16. Gomaa, H., Abd El-Monaem, E. M., Eltaweil, A. S. & Omer, A. M. Efficient removal of noxious methylene blue and crystal violet dyes at neutral conditions by reusable montmorillonite/NiFe2O4@amine-functionalized chitosan composite. *Sci. Rep.* **12**, 1–16 (2022).
17. Arunkumar, G. *et al.* Carbon encapsulated ZnO nanoplates for efficient removal of organic dyes from aqueous medium by adsorption: Role of organic ligand and calcination temperature. *J. Mol. Liq.* **403**, 124852 (2024).
18. Şenol, Z. M. *et al.* Removal of food dyes using biological materials via adsorption: A review. *Food Chem.* **450**, 139398 (2024).
19. Zhang, Q., Cheng, Y., Liu, C. & Fang, C. Electrochemical-driven removal of organic dyes by using bimetallic MOFs/waste cellulose acetate derived carbon foam as a freestanding electrode material. *J. Solid State Chem.* **330**, 124489 (2024).
20. Sukhadeve, G. K. *et al.* Visible light assisted photocatalytic degradation of Indigo Carmine dye and NO_2 removal by Fe doped TiO_2 nanoparticles. *Ceram. Int.* **48**, 29121–29135 (2022).
21. Bustos-Terrones, Y. A. *et al.* Removal of BB9 textile dye by biological, physical, chemical, and electrochemical treatments. *J. Taiwan Inst. Chem. Eng.* **121**, 29–37 (2021).
22. Pedebos, M. E. S. *et al.* Removal of Rhodamine B dye by adsorption onto an eco-friendly zeolite and machine learning modeling. *J. Photochem. Photobiol. A Chem.* **449**, 115404 (2024).
23. Dalmaz, A. & Sivrikaya Özak, S. Methylene blue dye efficient removal using activated carbon developed from waste cigarette butts: Adsorption, thermodynamic and kinetics. *Fuel* **372**, 132151 (2024).
24. Rasilingwani, T. E., Gumbo, J. R., Masindi, V. & Foteinis, S. Removal of Congo red dye from industrial effluents using metal oxide-clay nanocomposites: Insight into adsorption and precipitation mechanisms. *Water Resour. Ind.* **31**, 100253 (2024).
25. Ciğeroğlu, Z. *et al.* Clay-based nanomaterials and their adsorptive removal efficiency for dyes and antibiotics: A review. *Mater. Today Sustain.* **26**, 100735 (2024).
26. Akoulih, M. *et al.* Electrocoagulation-based AZO DYE (P4R) removal rate prediction model using deep learning. *Proc. Comput. Sci.* **236**, 51–58 (2024).
27. Tanti, M. & Patel, U. D. A synergistic application of simultaneous electrocoagulation-electrooxidation process for the treatment of floor-wash wastewater containing Rhodamine B dye. *J. Water Process Eng.* **56**, 104290 (2023).
28. Talaiekhozani, A., Reza Mosayebi, M., Fulazzaky, M. A., Eskandari, Z. & Sanayee, R. Combination of TiO_2 microreactor and electroflotation for organic pollutant removal from textile dyeing industry wastewater. *Alex. Eng. J.* **59**, 549–563 (2020).
29. Suliman, Z. A., Mecha, A. C. & Mwasiagi, J. I. Effect of TiO_2/Fe_2O_3 nanopowder synthesis method on visible light photocatalytic degradation of reactive blue dye. *Heliyon* **10**, e29648 (2024).
30. Zinatloo-Ajabshir, S. *et al.* Novel rod-like [Cu(phen)2(OAc)]·PF6 complex for high-performance visible-light-driven photocatalytic degradation of hazardous organic dyes: DFT approach, Hirshfeld and fingerprint plot analysis. *J. Environ. Manag.* **350**, 119545 (2024).
31. Zinatloo-Ajabshir, S., Morassaei, M. S. & Salavati-Niasari, M. Eco-friendly synthesis of Nd 2 Sn 2 O 7-based nanostructure materials using grape juice as green fuel as photocatalyst for the degradation of erythrosine. *Compos. Part B Eng.* **167**, 643–653 (2019).
32. Zinatloo-Ajabshir, S., Morassaei, M. S., Amiri, O. & Salavati-Niasari, M. Green synthesis of dysprosium stannate nanoparticles using *Ficus carica* extract as photocatalyst for the degradation of organic pollutants under visible irradiation. *Ceram. Int.* **46**, 6095–6107 (2020).
33. Zinatloo-Ajabshir, S., Mortazavi-Derazkola, S. & Salavati-Niasari, M. Schiff-base hydrothermal synthesis and characterization of Nd_2O_3 nanostructures for effective photocatalytic degradation of eriochrome black T dye as water contaminant. *J. Mater. Sci. Mater. Electron.* **28**, 17849–17859 (2017).

34. Zinatloo-Ajabshir, S. & Salavati-Niasari, M. Preparation of nanocrystalline cubic ZrO_2 with different shapes via a simple precipitation approach. *J. Mater. Sci. Mater. Electron.* **27**, 3918–3928 (2016).
35. Zinatloo-Ajabshir, S., Mortazavi-Derazkola, S. & Salavati-Niasari, M. Nd_2O_3–SiO_2 nanocomposites: A simple sonochemical preparation, characterization and photocatalytic activity. *Ultrason. Sonochem.* **42**, 171–182 (2018).
36. Zinatloo-Ajabshir, S., Mortazavi-Derazkola, S. & Salavati-Niasari, M. Preparation, characterization and photocatalytic degradation of methyl violet pollutant of holmium oxide nanostructures prepared through a facile precipitation method. *J. Mol. Liq.* **231**, 306–313 (2017).
37. Zinatloo-Ajabshir, S., Morassaei, M. S. & Salavati-Niasari, M. $Nd_2Sn_2O_7$ nanostructures as highly efficient visible light photocatalyst: Green synthesis using pomegranate juice and characterization. *J. Clean. Prod.* **198**, 11–18 (2018).
38. Khan, I., Shah, T., Tariq, M. R., Ahmad, M. & Zhang, B. Understanding the toxicity of trinitrophenol and promising decontamination strategies for its neutralization: Challenges and future perspectives. *J. Environ. Chem. Eng.* **12**, 112720 (2024).
39. Khan, N., Khan, I., Zada, N. & Saeed, K. Adsorption of Cu (II) ion through functionalized nylon 66 and their utilization as photocatalyst for the photodegradation of eriochrome black t dye in aqueous medium. *Fibers Polym.* **23**, 1266–1274 (2022).
40. Purnomo, A. S. *et al.* Anionic dye removal by immobilized bacteria into alginate-polyvinyl alcohol-bentonite matrix. *Heliyon* **10**, e27871 (2024).
41. Ting, A. S. Y., Cheng, C. K. W. & Santiago, K. A. A. Decolourization of malachite green dye by endolichenic fungi from the lichen Usnea sp.: A novel study on their dye removal potential. *J. King Saud Univ. Sci.* **33**, 101579 (2021).
42. Agha, H. M. *et al.* Enhancing cationic dye removal via biocomposite formation between chitosan and food grade algae: Optimization of algae loading and adsorption parameters. *Int. J. Biol. Macromol.* **258**, 128792 (2024).
43. Nyakairu, G. W. A. *et al.* Synthesis, characterization and application of Zeolite/Bi_2O_3 nanocomposite in removal of Rhodamine B dye from wastewater. *Clean. Water* **1**, 100004 (2024).
44. Alghanmi, R. M. & Abdelrahman, E. A. Simple production and characterization of ZnO/MgO nanocomposite as a highly effective adsorbent for eliminating congo red dye from water-based solutions. *Inorg. Chem. Commun.* **161**, 112137 (2024).
45. Al-Kadhi, N. S. *et al.* Calcium ferrite nanoparticles: A simple synthesis approach for the effective disposal of congo red dye from aqueous environments. *Inorganics* **12**, 69 (2024).
46. Yousefi, S. R., Alshamsi, H. A., Amiri, O. & Salavati-Niasari, M. Synthesis, characterization and application of Co/Co_3O_4 nanocomposites as an effective photocatalyst for discoloration of organic dye contaminants in wastewater and antibacterial properties. *J. Mol. Liq.* **337**, 116405 (2021).
47. Heidari-Asil, S. A. *et al.* Magnetically recyclable $ZnCo_2O_4$/Co_3O_4 nano-photocatalyst: Green combustion preparation, characterization and its application for enhanced degradation of contaminated water under sunlight. *Int. J. Hydrogen Energy* **47**, 16852–16861 (2022).
48. Alwan Altaa, S. H., Habeeb Alshamsi, H. A. & Jasim Al-Hayder, L. S. Synthesis and characterization of rgo/co3o4 composite as nanoadsorbent for rhodamine 6g dye removal. *Desalin. Water Treat.* **114**, 320–331 (2018).
49. Uddin, M. K. & Baig, U. Synthesis of Co_3O_4 nanoparticles and their performance towards methyl orange dye removal: Characterisation, adsorption and response surface methodology. *J. Clean. Prod.* **211**, 1141–1153 (2019).
50. Al-Wasidi, A. S., Hegazey, R. M. & Abdelrahman, E. A. Efficient removal of methylene blue dye from aqueous media using facilely synthesized magnesium borate/magnesium oxide nanostructures. *Molecules* **29**, 3392 (2024).
51. Alhalili, Z. & Abdelrahman, E. A. Facile synthesis and characterization of manganese ferrite nanoparticles for the successful removal of safranine T dye from aqueous solutions. *Inorganics* **12**, 30 (2024).
52. Chinoune, K. *et al.* Adsorption behavior of MB dye on alginate-sepiolite biocomposite beads: Adsorption, kinetics, and modeling. *Inorg. Chem. Commun.* **165**, 112558 (2024).
53. Saadi, A. S. *et al.* Efficient synthesis of magnetic activated carbon from oak pericarp for enhanced dye adsorption: A one-step approach. *Desalin. Water Treat.* **319**, 100420 (2024).
54. Nabieh, K. A., Mortada, W. I., Helmy, T. E., Kenawy, I. M. M. & Abou El-Reash, Y. G. Chemically modified rice husk as an effective adsorbent for removal of palladium ions. *Heliyon* **7**, e06062 (2021).
55. Al-Wasidi, A. S. & AlReshaidan, S. Enhanced removal of rhodamine b dye from aqueous media via adsorption on facilely synthesized zinc ferrite nanoparticles. *Inorganics* **12**, 191 (2024).
56. Abdelrahman, E. A. & Al-Farraj, E. S. Facile synthesis and characterizations of mixed metal oxide nanoparticles for the efficient photocatalytic degradation of rhodamine B and Congo red dyes. *Nanomaterials* **12**, 3992 (2022).
57. Almehizia, A. A. *et al.* Facile synthesis of copper carbonate/cobalt carbonate/manganese carbonate and copper oxide/cobalt manganese oxide/manganese oxide as novel nanocomposites for efficient photocatalytic degradation of crystal violet dye. *Int. J. Environ. Anal. Chem.* https://doi.org/10.1080/03067319.2022.2121164 (2022) (**in press**).
58. Abdelrahman, E. A. *et al.* Facile synthesis of MgO/CuO and MgO/Cu_3MgO_4 binary nanocomposites as promising adsorbents for the disposal of Zn(II) ions. *J. Inorg. Organomet. Polym. Mater.* **34**, 266–281 (2024).
59. Al-Wasidi, A. S. *et al.* Facile synthesis and characterisation of $Mn_{0.5}Zn_{0.5}Fe_2O_4$/Fe_2O_3 as a novel nanocomposite for studying analytical parameters affecting on photocatalytic degradation of basic fuchsin dye. *Int. J. Environ. Anal. Chem.* https://doi.org/10.1080/03067319.2022.2153044 (2022).
60. Al-Wasidi, A. S., Khairy, M., Abdulkhair, B. Y. & Abdelrahman, E. A. Efficient disposal of basic fuchsin dye from aqueous media using ZrO_2/$MgMn_2O_4$/$Mg(Mg_{0.333}Mn_{1.333})O_4$ as a novel and facilely synthesized nanocomposite. *Inorganics* **11**, 363 (2023).
61. Abdelrahman, E. A. *et al.* Efficient disposal of rhodamine 6G and acid orange 10 dyes from aqueous media using ZrO_2/$CdMn_2O_4$/CdO as novel and facilely synthesized nanocomposites. *Inorganics* **11**, 333 (2023).
62. Al-Wasidi, A. S. & Abdelrahman, E. A. Significant photocatalytic decomposition of malachite green dye in aqueous solutions utilizing facilely synthesized barium titanate nanoparticles. *Discov. Nano* **18**, 97 (2023).
63. Nulu, V., Nulu, A. & Sohn, K. Y. Room-temperature facile synthesis of Co_3O_4 nanoflakes as anode material for Li-ion rechargeable batteries. *Int. J. Electrochem. Sci.* **13**, 2069–2079 (2018).
64. Singh, V., Pandey, V., Singh, V. K. & Majhi, M. R. Synthesis and characterization of single-phase magnesium borate nanorod via solution reaction cum sintering process. *Ceram. Int.* **49**, 27086–27093 (2023).
65. Ozerova, A. M. *et al.* Cobalt borate catalysts for hydrogen production via hydrolysis of sodium borohydride. *J. Alloys Compd.* **513**, 266–272 (2012).
66. Alhalili, Z. & Abdelrahman, E. A. Efficient removal of Zn(II) ions from aqueous media using a facilely synthesized nanocomposite based on chitosan Schiff base. *Sci. Rep.* **14**, 1–15 (2024).
67. Al-wasidi, A. S., Shah, R. K. & Abdelrahman, E. A. Facile synthesis of $CuFe_2O_4$ nanoparticles for efficient removal of acid blue 113 and malachite green dyes from aqueous media. *Inorganics* **12**, 143 (2024).
68. Al-Wasidi, A. S. & Abdelrahman, E. A. Functionalization of strontium ferrite nanoparticles with novel chitosan-schiff base ligand for efficient removal of Pb(II) ions from aqueous media. *Inorganics* **12**, 148 (2024).
69. Shafeeq, K. *et al.* Functionalization of calcium silicate/sodium calcium silicate nanostructures with chitosan and chitosan/glutaraldehyde as novel nanocomposites for the efficient adsorption of Cd(II) and Cu(II) ions from aqueous solutions. *Silicon* **16**, 1713–1730 (2024).
70. Al-Kadhi, N. S. *et al.* A facile sol-gel synthesis and characterization of $MgCO_3$/$MnCO_3$ and $MgMn_2O_4$/Mn_2O_3 novel nanostructures with remarkably high adsorption activity toward eriochrome black T dye. *J. Inorg. Organomet. Polym. Mater.* **33**, 2046–2057 (2023).

71. Ahamad, Z. & Nasar, A. Polypyrrole-decorated bentonite magnetic nanocomposite: A green approach for adsorption of anionic methyl orange and cationic crystal violet dyes from contaminated water. *Environ. Res.* **247**, 118193 (2024).
72. Shirsath, S. R., Patil, A. P., Bhanvase, B. A. & Sonawane, S. H. Ultrasonically prepared poly(acrylamide)-kaolin composite hydrogel for removal of crystal violet dye from wastewater. *J. Environ. Chem. Eng.* **3**, 1152–1162 (2015).
73. Sarabadan, M., Bashiri, H. & Mousavi, S. M. Removal of crystal violet dye by an efficient and low cost adsorbent: Modeling, kinetic, equilibrium and thermodynamic studies. *Korean J. Chem. Eng.* **36**, 1575–1586 (2019).
74. Gholami, M., Vardini, M. T. & Mahdavinia, G. R. Investigation of the effect of magnetic particles on the Crystal Violet adsorption onto a novel nanocomposite based on κ-carrageenan-g-poly(methacrylic acid). *Carbohydr. Polym.* **136**, 772–781 (2016).
75. Muthukumaran, C., Sivakumar, V. M. & Thirumarimurugan, M. Adsorption isotherms and kinetic studies of crystal violet dye removal from aqueous solution using surfactant modified magnetic nanoadsorbent. *J. Taiwan Inst. Chem. Eng.* **63**, 354–362 (2016).
76. Gupta, S., Prajapati, A., Kumar, A. & Acharya, S. Synthesis of silica aerogel and its application for removal of crystal violet dye by adsorption. *Watershed Ecol. Environ.* **5**, 241–254 (2023).
77. Rath, J. *et al.* Green synthesis of silver nanoparticles decorated on graphene oxide for crystal violet dye removal. *Diam. Relat. Mater.* **146**, 111192 (2024).
78. Foroutan, R., Peighambardoust, S. J., Peighambardoust, S. H., Pateiro, M. & Lorenzo, J. M. Adsorption of crystal violet dye using activated carbon of lemon wood and activated carbon/Fe_3O_4 magnetic nanocomposite from aqueous solutions: A kinetic, equilibrium and thermodynamic study. *Molecules* **26**, 1–19 (2021).
79. Chakraborty, S. *et al.* Study on isotherm, kinetics, and thermodynamics of adsorption of crystal violet dye by calcium oxide modified fly ash. *Environ. Eng. Res.* **26**, 1–9 (2021).
80. Albo Hay Allah, M. A., Ibrahim, H. K., Alshamsi, H. A. & Radhi Saud, H. Eco-friendly synthesis of biochar supported with zinc oxide as a heterogeneous catalyst for photocatalytic decontamination of Rhodamine B under sunlight illumination. *J. Photochem. Photobiol. A Chem.* **449**, 115413 (2024).

Acknowledgements

The authors are grateful to Princess Nourah bint Abdulrahman University, Riyadh, Saudi Arabia for funding this work through Researchers Supporting Project number (PNURSP2024R35).

Author contributions

A.S.A.-W.: Funding acquisition, writing—review and editing, H.H.E.-F.: Methodology, R.K.S.: Writing—review and editing, F.A.S.: Writing—review and editing, E.A.A.: Methodology, writing—review and editing, conceptualization.

Funding

This research was funded by Princess Nourah bint Abdulrahman University Researchers Supporting Project number (PNURSP2024R35), Princess Nourah bint Abdulrahman University, Riyadh, Saudi Arabia.

Competing interests

The authors declare no competing interests.

Institutional review board statement

The authors ensure that the paper hereby submitted is completely original and has not been previously published in any format or language, either partially or in its complete form anywhere else. This study was conducted and approved according to the guidelines of the Declaration of the Ethical Committee of the Faculty of Science, Benha University (No. BuFs-REC-2024-199 Chm).

Additional information

Correspondence and requests for materials should be addressed to H.H.E.-F. or E.A.A.